Color and Spatial Frequency Provide Functional Signatures of Retinotopic Visual Areas

Spencer R. Loggia [1], Stuart J. Duffield [1], Kurt Braunlich [1,2], and Bevil R. Conway [1,✉]

[1]National Eye Institute

[2]National Institute of Mental Health

The visual cortex contains multiple retinotopic representations of the visual field. A long-standing question of visual neuroscience concerns the role of these different regions in visual computations and perception. Differences in psychophysical properties have also been noted across the visual field, varying with eccentricity and with the upper and lower hemifields. Inspired by studies that used linear-systems-defined stimuli to characterize single neuron responses, we collected fMRI data from two macaque monkeys as they passively viewed gratings that varied in color, saturation, and spatial frequency. We apply a novel variant of multivariate linear discriminant analysis to discover combinations of these features that best separated visual cortex, along three dimensions of representation: eccentricity; classic retinotopic progression (V1, V2, V3, V3a, V4, MT+); and upper vs lower visual field. As expected from prior work, eccentricity across all visual areas was characterized by responses to color and spatial frequency: foveal regions, compared to peripheral regions, showed greater responses to colors not restricted to the S-cone-axis and high spatial frequency. Retinotopic visual areas were characterized by their responses to saturation: relative to anterior visual areas (V3-V4, V3a, MT+), posterior areas (V1-V2) were more responsive to increases in saturation. And upper-vs-lower representations were distinguished by responses to colors modulating along the Daylight locus: ventral areas showed relatively higher responses to colors associated with the Daylight locus (orange/blue) as compared to responses to achromatic luminance. Together, these results provide a data driven approach that recovers functional signatures of retinotopic organization using color and spatial frequency, providing clues toward the different roles that the components of retinotopic cortex play in visual perception.

Color | Visual Neuroscience | Macaque | Retinotopy

Correspondence: *bevil.conway@nih.gov*

Introduction

Color is a fundamental component of vision, influencing object and scene identification (Callaghan, 1984; Gegenfurtner and Rieger, 2000; Witzel and Gegenfurtner, 2018), as well as sexual selection and foraging behavior (Sumner and Mollon, 2000; Surridge et al., 2003). In both humans and and macaques, color processing begins in the retina, where distinct cone classes process short, medium and long wavelengths of light (Stockman and Sharpe, 2000). This chromatic information is further processed by other cells in the retina, the lateral geniculate nucleus, and then retinotopic areas in the visual cortex (V1, V2, V3, V4) (Essen and Zeki, 1978; Van Essen, 2004; Wandell and Winawer, 2011; Zeki et al., 1991; Mullen, 2019; Wade et al., 2008, 2002; Conway, 2009; Horwitz, 2020). Multiple color-biased regions are also found in inferior temporal cortex, in both human (Lafer-Sousa et al., 2016; Beauchamp et al., 1999; Pennock et al., 2022; Cant and Goodale, 2006) and macaque (Lafer-Sousa and Conway, 2013; Harada et al., 2009). These color selective regions are organized in both species such that color-biased regions are sandwiched between face and place selective regions.

The role that different cortical regions play in visual perception remains poorly understood. One intriguing hypothesis is that color is exploited by different visual regions for different visual computations. If this is the case, then cortical regions might be expected to respond differently to colored stimuli. (Rosenthal et al., 2018), for example, reported that the color-tuning of inferior temporal (IT) cortex correlates with the color statistics of parts of scenes labeled as objects, and color-biased regions appear to be selective for the colors of food (Pennock et al., 2022; Khosla et al., 2022). Differences in color preference across visual field eccentricity is also consistent with the hypothesis that color contributes differently across the visual field. Sensitivity to LM contrast drops off rapidly with eccentricity, while sensitivity to S contrast remains fairly stable across the visual field, shown both psychophysically and with fMRI (Mullen et al., 2005; D'Souza et al., 2016), and matching expectations based on photoreceptor distributions in the retina (Cornish et al., 2004). In the present work, we aim to further test this hypothesis, using a data-driven approach to evaluate the extent to which differences in responses to colored gratings can be used to characterize visual cortical regions. In addition, behavioral studies show differences in perception across upper and lower visual field in humans (Zito et al., 2016).

Substantial information about the mechanisms of vision has been gained by measuring behavioral and neural responses to colored gratings that vary in spatial frequency, following a linear-systems approach used to characterize psychophysical performance and neural responses in the visual system (Enroth-Cugell and Robson, 1966; Movshon et al., 1978; Lennie et al., 1990; Horwitz et al., 2005; Johnson et al., 2004; Hass et al., 2015). This approach has also facilitated the comparison of perceptual performance with brain responses obtained with functional magnetic resonance imaging (fMRI) in humans (Singh et al., 2000; Wade et al., 2002; Liu and Wandell, 2005; Brewer et al.,

2005; Pihlaja et al., 2008; Mullen, 2019), and macaque monkeys (Wade et al., 2008), an important animal model of the human case.

To better understand how representations of color differ between cortical regions, we used whole-brain fMRI in macaques to examine how representations of spatial frequency, hue, and saturation differ by cortical area. We identify the most salient differences in responses through a novel variant of multivariate Linear Discriminant Analysis, which finds sparse and simple combinations of stimuli that maximize variance between the voxels of different cortical regions and minimize variance between the voxels within a cortical region. The overarching motivation for these experiments is twofold. First, we assess the extent to which retinotopically defined regions (V1, V2, V3, V3a, V4, and MT+) and their visual field representations (upper versus lower visual field and central versus peripheral visual field) can be distinguished by responses to simple colored and grayscale grating stimuli. This assessment is relevant to questions about the contribution of different areas to visual processing, and how color is used at different stages. Second, we seek to determine the extent to which the macaque is a model of the human case by comparing our results to previously published work obtained in humans. Comparing brain structures and function across macaques and humans is important not only for establishing the limits of the macaque as a model system, but also for understanding the evolutionary history of primate brains. (Kaas, 1993; Rosa and Tweedale, 2005; Kaas, 2013; Rilling, 2014; Lafer-Sousa et al., 2016; Conway, 2018).

Methods

Functional Magnetic Resonance Imaging Acquisition

Imaging acquisition was the same as in (Lafer-Sousa et al., 2012; Lafer-Sousa and Conway, 2013). Some of the data analyzed presently was used in prior publications, and other data has not previously been analyzed; the data will be available open-access at neicommons (https://neicommons.nei.nih.gov). Two rhesus macaques (7-8 kg, M1 and M2), were scanned at the Martinos Imaging Center at Massachusetts General Hospital (MGH) in a 3 Tesla Allegra (Siemens, New York, New York) scanner using a custom-made four-channel send-receive surface coil (Martinos Center, MGH, Charlestown, Massachusetts). Images were acquired using standard Echo-Planar Imaging (EPI) methods, with 2 second repetition time (TR), each repetition acquiring a 98 x 63 x 98 voxel matrix with 1mm isotropic voxels. Animals were trained, using juice rewards, to sit in a sphinx position in a custom-built plastic chair placed inside the bore of a horizontal scanner while fixating a central target on a display screen. Head position was maintained with custom plastic head posts that were surgically implanted (see surgical methods, (Lafer-Sousa et al., 2012)). Eye movements were tracked with an infrared eye tracker (ISCAN, Burlington, Massachusetts). Animals were rewarded for maintaining fixation within a degree of the central fixation target. Microparticular iron oxide agent (MION), Feraheme (AMAG Pharmaceuticals, Cambridge, Massachusetts), was injected intravenously in the saphenous vein immediately prior to scanning to improve the magnetic resonance signal (8-10 mg/kg, diluted in approximately equal volume of saline). High-resolution anatomical scans (0.35 mm x 0.35 mm x 0.35 mm in M1 and 0.35 mm x 0.4 mm x 0.35 mm in M2) were obtained while the animals were lightly sedated during a separate scanning session. All imaging and surgical procedures follow local and National Institute of Health guidelines. All imaging and surgical procedures were approved by the Harvard Medical School Institutional Animal Care and Use Committee.

Experimental Design

Four fMRI experiments were conducted over the course of 6-7 sessions (7 sessions in M1, 6 sessions in M2). Each scan session consisted of 13-24 stimulus runs, details of which are described below.

For all fMRI experiments, visual stimuli were presented on a screen 48.2 cm away from the subject with a JVC DKLA projector at 1024x768 pixel resolution. For experiments 1, 3, and 4, the projected image subtended a 22.5 cm by 16.9 cm area (27 DvA by 20 DvA) on the screen, and for experiment 2 the projected image subtended a 35 cm by 26.8 cm area (41 DvA by 31 DvA). The projector's luminance output was linearized, and colors were measured and calibrated using spectral readings taken from a PR-655 (Photo Research, Inc, Chatsworth, California). Spectra were multiplied by the Judd-revised CIE 1931 color matching functions to derive CIE xyY coordinates of the colors as displayed by the monitor phosphors (Figure 1b). Stimuli filled the entire screen and contained a small fixation

cross at the center. All stimuli were presented in a blocked paradigm.

The colors of the gratings in experiment 3 and 4 were defined in the physiologically relevant DKL-MB color space (Derrington et al., 1984; MacLeod and Boynton, 1979), which is defined by axes representing color tuning in the LGN (Figure 1a). These axes consist of two equiluminant color opponent axes, the L-M axis (demarcated in Figure 1a by color angles 0 and 180) and the S-(L+M) axis (demarked by color angles 90 and 270), as well as the luminance axis (Figure 1a, insert), which is modulated by the combined response of the L, M, and S cones. Colors in each experiment either modulated along the the L-M axis, the S-(L+M) axis, the luminance axis, or two intermediate axes, the (+L-M)-S / (-L+M)+S) Daylight or Orange-Cyan axis (45 and 225 degrees), and the (-L+M)-S / (+L-M)+S) Antidaylight or Green-Magenta axis (135 and 315 degrees). We refer to these five axes as LM, S, LMS, Daylight, and Antidaylight respectively throughout, following a convention established by others (Goddard et al., 2010b) and (Lafer-Sousa et al., 2012). The limits of the DKL-MB colorspace are bounded by the monitor, with the closest intersection of the LM and S axes with the monitor gamut defining the maximum cone-opponency with respect to the graypoint (Figure 1b).

The first experiment was a retinotopic mapping experiment (Experiment 1, Figure 2a), in which areas of visual cortex responsive to the horizontal and vertical meridians of the visual field were identified. Stimuli consisted of black-and-white checkerboard wedges that flickered between complementary checkerboard patterns every 1 second. Stimuli were presented in blocks, and blocks consisted either of two wedges radiating from the central fixation spot and spanning the vertical meridian of the screen, two wedges spanning the horizontal meridian of the screen, or the background gray, which was presented after each meridian block. Blocks consisted of 32 seconds (16TRs) and each run had 16 blocks, resulting in 512-second-long runs. For all runs, the conditions were ordered Horizontal, Gray, Vertical, Gray, repeated four times. A total of 13 runs of this experiment were collected in M1, and 14 runs were collected in M2.

The second experiment was an eccentricity mapping experiment (Experiment 2, Figure 2b). Stimuli consisted of LMS, LM, or S checkerboards presented in rings centered on the fixation point; the checkerboards flickered between complementary checkerboard patterns every 1 second. Rings extended from the fovea to 13.4 degrees of visual angle (DvA), with each successively larger ring having an inner radius equal to the outer radius of the previous ring. Rings possessed outer radii of 1.5, 3.5, 7, 13.4 degrees of visual angle (DvA). Blocks consisted of either one of the rings or the gray background, which was presented after each ring block. Blocks consisted of 32 seconds (16 TRs) and each run had 17 blocks, resulting in 544-second-long runs. For all runs, the conditions were ordered Gray, 1.5 degrees, Gray, 3.5 degrees, Gray, 7 degrees, Gray, 13.4 degrees, repeated twice, with a final gray block. A total of 24 runs were collected in M1 and 21 runs were collected in M2.

The third experiment presented color-gray trapezoidal gratings with a spatial frequency of 0.48 cycles per degree (CpD) (Experiment 3, Figure 1c). The 'flat' (color or gray) portions of the gratings spanned 80% of each cycle.

Separate stimuli were generated for each pole of the four color axes (LM, S, Daylight, and Antidaylight) yielding a total of 8 color-gray gratings; each grating was presented at four saturation levels, defined as 10%, 30%, 50%, or 95% of the saturation of the display defined in the DKL-MB colorspace (see Supplementary Table 1 for the cone contrasts for each color). Color-pairs along the Daylight axis had the same absolute spatiotemporal Michelson cone contrast as the color-pairs along the Antidaylight axis (Supplementary Table 2). The gratings drifted right-to-left or left-to-right at a speed of 0.8 cycles per second, and the direction of the drift changed every two seconds. The LMS gratings possessed 1%, 2.5%, 5.5%, or 8.7% luminance contrast (Supplementary Table 1). Blocks of gratings were interleaved with blocks of gray. The experiment had blocks of 28 seconds (14 TRs) and each run had 19 blocks, resulting in 532-second-long runs. Block orders were counterbalanced to minimize order effects, while also minimizing design predictability for the color-gray gratings. Grayscale gratings appeared in the middle of the sequence of blocks in each run. A total of 49 runs were collected in M1, and 58 runs were collected in M2. The number of times each block type was presented varied between 26 and 28.

The fourth experiment presented heterochromatic gratings (each phase defined one pole of a given color axis, using the LM and S axes) and LMS gratings with a spatial frequency of either 0.2 CpD, 4 CpD, or 8 CpD (Experiment 4, Figure 1d). The colors of the heterochromatic gratings were set at 90% of the saturation of the display defined in the DKL-MB colorspace, and the two sets of LMS gratings had either 90% or 9% luminance contrast, respectively. Blocks of gratings were interleaved with blocks of gray. The gratings flickered between complementary patterns every one second. The experiment had blocks of 32 seconds (16 TRs) and each run had 25 blocks, resulting in 800-second-long runs. Block orders were counterbalanced to minimize order effects, while also minimizing design predictability. A total of 14 runs were collected in M1, and 13 runs were collected in M2. Each block type was presented 27 times.

fMRI Preprocessing

The raw data was unpacked from DICOM to NIFTI format using dcm2niix (https://github.com/rordenlab/dcm2niix). The images underwent thermal denoising using PCA algorithms (Vizioli et al., 2021), which improved the signal to noise ratio of the functional images. Images were reoriented from the sphinx position. Data was motion corrected with FSL's MCFLIRT motion correction algorithm with 12 degrees of freedom. The functional volumes were then linearly coregistered to the anatomical volumes using ITK-SNAP (http://www.itksnap.org/) and ANTs non-linear registration algorithm (ANTs, http://stnava.github.io/ANTs) to get the closest mapping of the functional volumes to the anatomical image. Nilearn's GLM module (https://nilearn.github.io/) was used to calculate β coefficients and create statistical contrast maps, using drift regressors up to the 3rd order polynomial to account for fMRI signal drift. Blocks were modeled as boxcars of appropriate duration, and convolved with the MION hemodynamic response function (HRF) (Vanduffel et al., 2001). No spatial smoothing was applied.

Anatomical Processing and Region of Interest Definition

To create surfaces of the macaque brain for visualization, the high-resolution anatomical images were skull-stripped, white matter regions were labeled, and surfaces were generated and inflated with FreeSurfer (http://surfer.nmr.mgh.harvard.edu/).

To define retinotopic areas, the significance maps of the contrast between the vertical and horizontal cortical areas were displayed on the inflated surface of each subject and the boundaries of the retinotopic areas were defined at the vertical or horizontal meridians, depending on whether the area of interest subtended a quarterfield or hemifield of visual area. Surface labels of the retinotopic areas were transformed into the anatomical volume space. These retinotopic areas were cross-referenced with the both the D99 macaque atlas (https://afni.nimh.nih.gov/) (Reveley et al., 2016), which was registered to each subject's anatomical space, and an illustrated atlas (Paxinos et al., 2000), and edited to produce the final retinotopic regions of interest for each subject (Figure 1a). Due to it lacking complete retinotopic borders from our experiment, MT+ (the MT cluster, including MT, FST, MST, and V4t), was produced entirely from the D99 and Paxinos atlases. The resulting MT cluster, in accordance with previous literature, features a continuous eccentricity map in a three-quarters circle around the foveal representation in the superior temporal sulcus, suggesting it closely maps to its retinotopic boundaries (Figure 2b) (Kolster et al., 2009).

Retinotopic regions were further delineated into dorsal and ventral ROIs by drawing to a line through the horizontal meridian of V1 and through the center of the foveal confluence on each subject's surface, dividing each hemisphere into dorsal and ventral portions. These surface labels were then back-projected into anatomical space, and used as a reference to divide the retinotopic ROIs into ventral and dorsal regions. V3a and MT+, being located on the dorsal surface of the cortex, were not subdivided, despite these areas having representations of the upper and lower visual field (Gattass et al., 1988; Kolster et al., 2009).

To determine eccentricity-preferring regions, statistical contrasts between neighboring rings were generated, and voxels were assigned to eccentricities depending on their z-score, moving outward from foveal regions to the periphery (Figure 1b).

Sparse Linear Discriminant Analysis (sLDA)

To identify composite features that would separate retinotopic areas, we apply a variant of Linear Discriminant Analysis (LDA). We use it to answer the question "What simple combinations of the features separate the voxels in such a way that they naturally cluster into a given set of ROIs?"

Standard implementations of LDA find a projection hyperplane that maximizes the distance between classes while minimizing intra-class variance analytically, via eigendecomposition (Xanthopoulos et al., 2013). Our

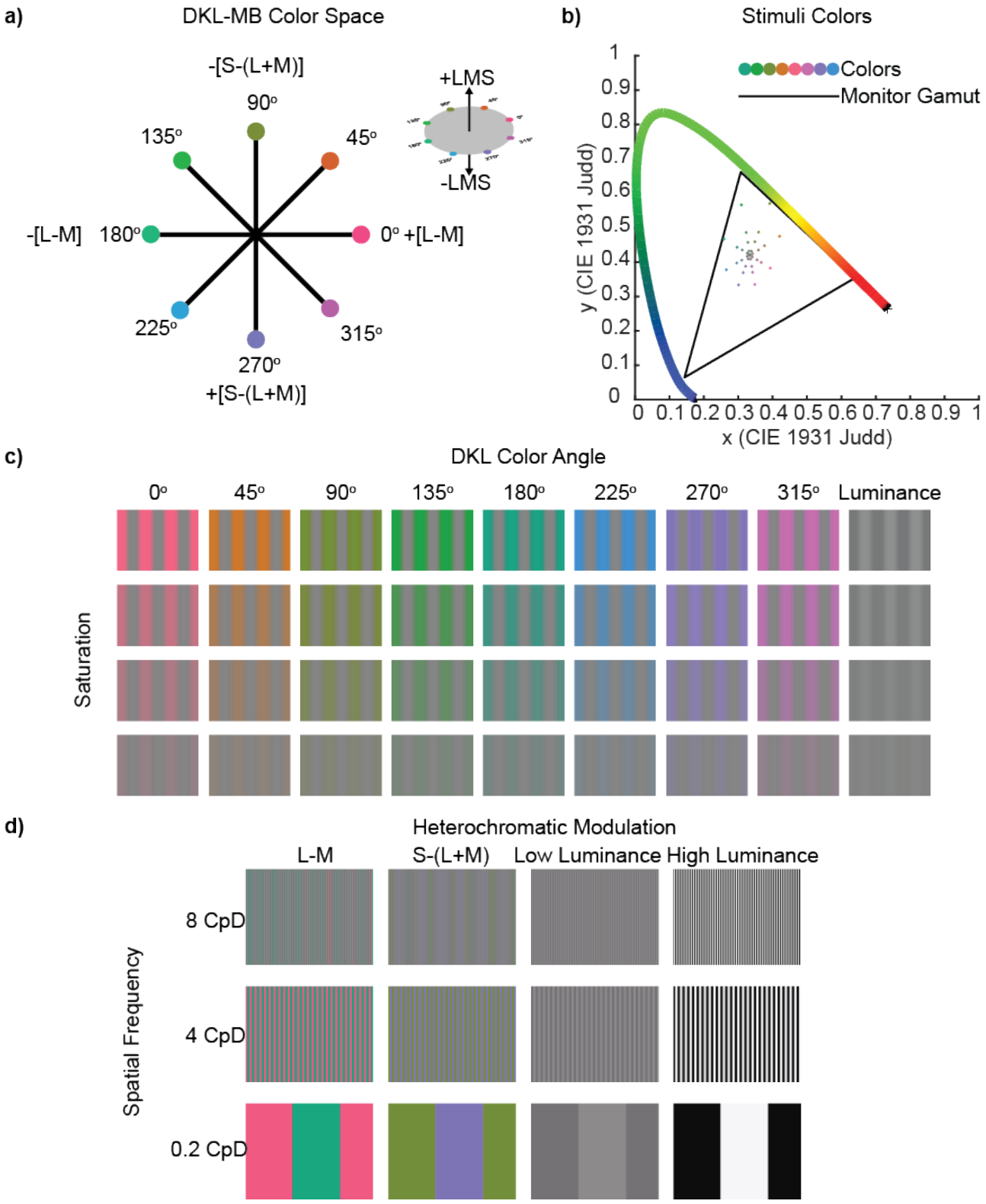

Figure 1. Overview of the colors and stimuli presented in the two gratings experiments. **a)** An equiluminant plane DKL-MB colorspace, in which the colors of the grating stimuli were generated. Colors modulated along 5 axes in this color space, LM (0 and 180 degrees), Daylight (45 and 225 degrees), S (90 and 270 degrees), Antidaylight (135 and 315 degrees), and LMS, which extends orthoganally to the equiluminant plane, as shown to the right. **b)** Colors used in experiment 3 as measured in CIE-1931 chromaticity diagram. **c)** Representations of stimuli as presented in experiment 3, showing LMS (Luminance), S (90 and 270), LM (0 and 180), Daylight (45 and 225), and Antidaylight (135 and 315) gratings at different saturations. The spatial frequencies of the gratings shown here are 8 times lower than the actual presented frequencies for the purposes of illustration. **d)** Representations of stimuli presented in experiment 4, showing LMS, S, and LM gratings at different spatial frequencies. The spatial frequencies of the gratings shown here are 8 times lower than the actual presented frequencies.

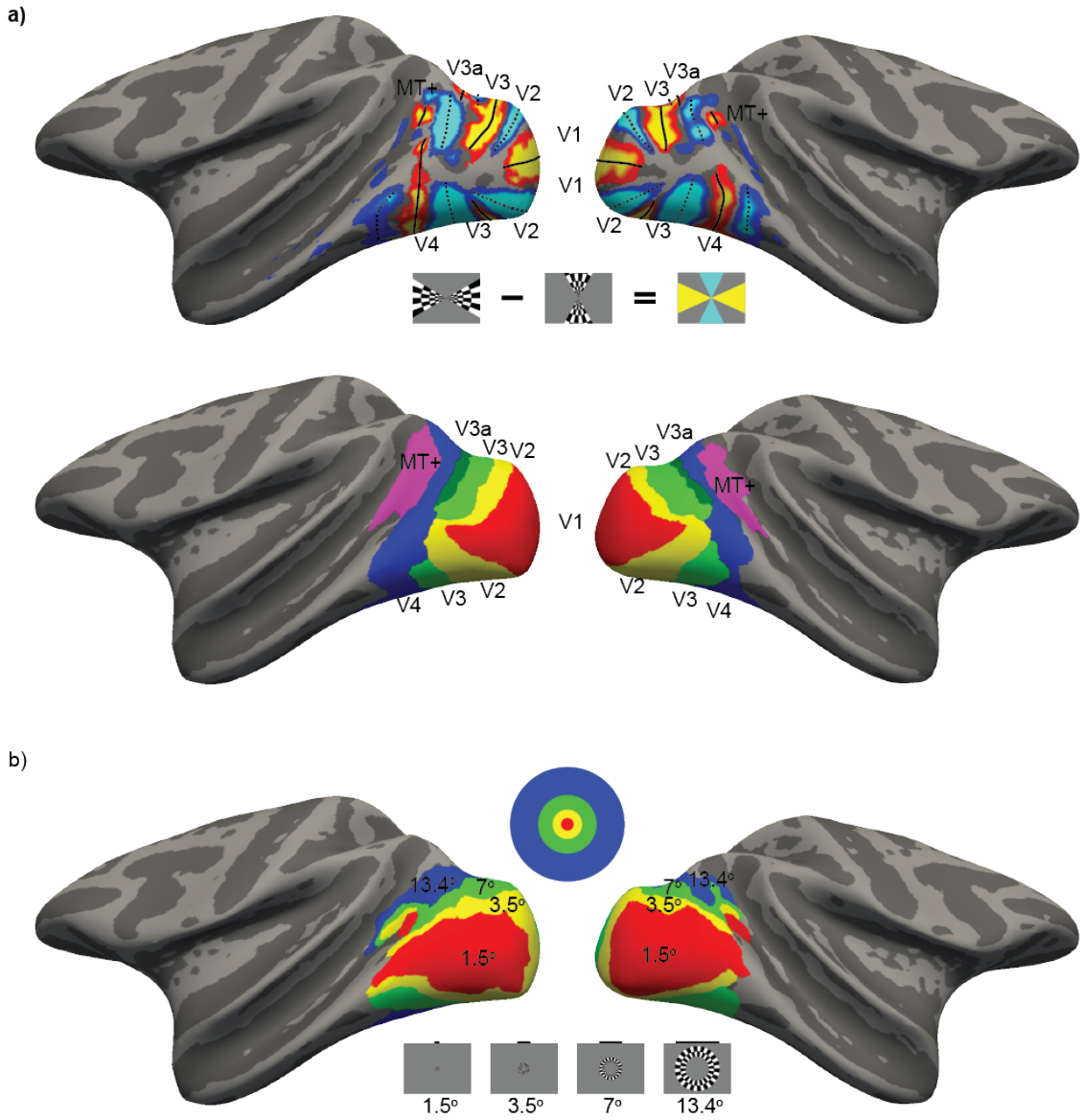

Figure 2. An overview of the retinotopic mapping experiments and the cortical parcellation of the brain into retinotopic and eccentricity-preferring areas. **a)** To functionally delineate retinotopic areas in each macaque individually, the animals were shown vertically and horizontally oriented checkerboard wedges in a blocked paradigm. The contrast maps between these two conditions displayed on the inflated surface of M1 reveal the borders of the retinotopic areas along the vertical (blue) and horizontal (red) meridians, depending if the given area has a hemifield or quarterfield representation. An illustration of the contrast is shown with stimuli from the experiment below the contrast map. The final parcellation for the retinotopic ROIs are shown on the surfaces beneath the contrast maps. The same data was used in (Lafer-Sousa et al., 2012; Lafer-Sousa and Conway, 2013) for cortical parcellation. **b)** To functionally delineate eccentricity regions, checkerboard rings and circles were presented in a blocked paradigm, and the statistical contrasts between these conditions were used to parcellate foveal and peripheral regions. The final parcellation for these regions are shown here for M1. Two eccentricity maps bordering three-quarters of a foveal confluence can be seen, representing the eccentricity maps of the V1-V4 cluster and the MT cluster according to previous literature (Kolster et al., 2009).

implementation adds L1 regularization of discriminant vectors offer finer control over the objective function, and thus must be solved numerically.

Given number of voxels v, number of stimulus conditions m and number component vectors k, the model uses a $(m \times k)$ linear transform matrix T to take the input data matrix (in this case a $v \times m$ standardized β coefficient matrix) into a k dimensional euclidean space. We find a T that maximizes the pairwise distance between class (ROI label) centers, while minimizing variance within those classes, and making T as sparse as possible. Explicitly, we find:

$$\underset{T}{\textbf{argmin}} \quad -\sum_{\forall f_1 \in R} \sum_{\forall f_2 \in R} \frac{M_{f_1,f_2} \sqrt{\sum_k (\overline{\beta_{f_1} T} - \overline{\beta_{f_2} T})^2}}{|R|^2} + \sum_{\forall f \in R} \frac{(\beta_f T - \overline{\beta_f T})^2}{(|f|-1)|R|} + S \sum |T| \tag{1}$$

Where R is the set of ROI labels (and $|R|$ is the number of ROIs), T is the transform we are trying to discover (the set of k length m component vectors), β is the beta matrix with m features, k is the number of target components or dimensions, and M is a weight matrix that allows control over the importance of separating each pair of classes. Here, M is used exclusively as a binary mask. This objective is optimized via gradient decent, specifically, we use the ADAM optimization method (Kingma and Ba, 2014). The first term computes the distance in the target space between the centers of each class. The second term is simply the total covariance within each class. It ensures that observations assigned the same class remain tightly grouped. The third term encourages sparsity of the matrix T, and is scaled by hyperparameter S. This is useful for encouraging the model to find simple, interpretable embedding features. Error in the LDA model can be established by bootstrapping. The model is fit on 100 independent resamplings with replacement of all fMRI runs. Variance and expected value for each class is determined by fitting a normal distribution over all resamplings.

β coefficients derived from Nilearn's general linear model fit to the data from experiments 3 and 4 in both subjects were standardized and concatenated, resulting in a Voxels $\times$ Conditions matrix. Each voxel was assigned to a visual area, half-area (ventral/dorsal), and eccentricity. First the sLDA model was fit on the left and right hemisphere data independently across both subjects and all eccentricities, that is each index of weight parameter M was 1. Next, in order to avoid the potentially confounding impact of visual field eccentricity, the sLDA model was fit ignoring distances across eccentricities, by setting the corresponding indexes in M to zero.

Cortical surface representations of the LDA components were constructed using effect-size contrasts in Nilearn and projected onto the inflated surface of M1. In the effect-size contrasts, the contribution of all components were equal, and do not reflect the weighting of each feature in the LDA components.

The nomenclature for the conditions that make up the composite LDA features changes slightly for the sake of brevity in the figures, and some conditions are excluded due to their responses being too similar to the constant coefficient to be informative. Table 1 lists the LDA conditions and what gratings they correspond to.

Feature Nomenclature	Grating Description(s)
LM_high_sat	DKL 0 95% Saturation, DKL 180 95% Saturation
LM_med_sat	DKL 0 50% Saturation, DKL 180 50% Saturation
LM_low_sat	DKL 0 30% Saturation, DKL 180 30% Saturation
S_high_sat	DKL 90 95% Saturation, DKL 270 95% Saturation
S_med_sat	DKL 90 50% Saturation, DKL 270 50% Saturation
S_low_sat	DKL 90 30% Saturation, DKL 270 30% Saturation
Daylight_high_sat	DKL 45 95% Saturation, DKL 225 95% Saturation
Daylight_med_sat	DKL 45 50% Saturation, DKL 225 50% Saturation
Daylight_low_sat	DKL 45 30% Saturation, DKL 225 30% Saturation
Antidaylight_high_sat	DKL 135 95% Saturation, DKL 315 95% Saturation
Antidaylight_med_sat	DKL 135 50% Saturation, DKL 315 50% Saturation
Antidaylight_low_sat	DKL 135 30% Saturation, DKL 315 30% Saturation
LMS_high_sat	LMS 8.7% Luminance Contrast
LMS_med_sat	LMS 5.5% Luminance Contrast
LMS_low_sat	LMS 2.5% Luminance Contrast
LM_high_freq	LM 8 CpD
LM_low_frew	LM 0.2 CpD
S_high_freq	S 8 CpD
S_low_freq	S 0.2 CpD
LMS_high_freq	High Luminance 8 CpD
LMS_low_freq	High Luminance 0.2 CpD

Table 1. Conditions corresponding to feature names used in display of sLDA discriminant / component vectors.

Univariate Analysis

For univariate analyses, β coefficients for each condition were divided by the β coefficient for the constant term in each voxel and multiplied by 100 to derive approximations of signal change. β coefficients were averaged across both subjects, weighted according to the number of times they observed each condition. For error estimation, β coefficients were bootstrapped across runs 100 times, resampling from the runs of both subjects with replacement, and normal distributions were fit to the bootstrapped samples. Signal change and error estimation was calculated for each ROI separately.

Since the LM, S, Daylight, and Antidaylight features investigated are composed of two different colored gratings for each saturation level, the signal change and the error of these features were calculated by taking the mean of the signal change for the two grating conditions that composed these features and by propagating the error of the two grating conditions using standard formulas.

Contrast response function and eccentricity response function slopes were calculated by fitting a linear regression to the signal change of each ROI as a function of saturation or eccentricity, respectively.

Surgical Procedures

Surgical methods are the same as (Lafer-Sousa et al., 2012). All surgical procedures follow local and National Institute of Health guidelines. All surgical procedures were approved by the Harvard Medical School Institutional

Animal Care and Use Committee.

Results

To see whether simple combinations of low-level visual features, such as color and spatial frequency, could differentiate retinotopic areas, we fit our sparse Linear Discriminant Analysis (sLDA) model to the data, using ROI and eccentricity preferences as labels. The sLDA model tries to find a sparse linear transformation T of the β coefficients for each condition that maximizes pairwise distance between class (ROI) centers while minimizing variances within each class (see methods).

We plot the ROI labels along the top two components, with the shape of each point indicating the ROI, cross-hatching indicating dorsal/ventral location, and shading indicating eccentricity (Figure 3a). The data from the left and right hemispheres are plotted separately to give a sense of the reliability of the embedding model. Within each ROI there appears to be a organization based on eccentricity along component 2. More peripheral voxels tend to have lower values, and voxels closer to the fovea tend to have higher values. Positive values on component 2 indicate response to Antidaylight, LM, and high frequency LMS gratings, and negative values indicate response to lower frequency LMS and S gratings. There also appears to be some organization of different ROIs with respect to color along component 1 and 2, with more anterior and dorsal regions having higher values and lower values along component 1 and 2, respectively, although this relationship is less clear.

To clarify the relationships found by the LDA components, we further investigate how foveal and peripheral regions can be separated using univariate analysis. In Figure 3c we directly compare color response across frequency and eccentricities. This shows the same relationship observed with sLDA. Response to medium and high frequency LM and high frequency gratings decrease with eccentricity, while response to S gratings is stable or trends towards increasing with eccentricity for all spatial frequencies, and had significantly greater slopes than LM medium frequency, LM high frequency, and LMS high frequency gratings. (1-tailed t-tests: LM 4 CpD slope < S 4 CpD slope p=0.0192; LM 8 CpD < S 8 CpD slope, p=0.0074; LMS 8 CpD slope < S 8 CpD slope p=0.0078). This also agrees with extensive psychophysical and fMRI work in humans (Mullen et al., 2005, 2007).

To find components that more clearly differentiate retinotopic regions, we fit the sLDA model again using only information within eccentricity levels (Figure 4). This reveals a clear functional organization from anterior to posterior visual areas and from ventral to dorsal visual areas (upper to lower visual hemifield). Posterior-anterior position of a retinotopic area can be discerned from its positioning along the axis of component 1, with V1 consistently having low values across all eccentricities and MT+ having high values across all eccentricities, and intermediate regions aligning themselves between them. The weight vector for component 1 (Figure 4b) suggests that this anterior/posterior split may be predominantly driven by difference between high and low cone contrast stimuli. We visualize this in figure 4c, effect-size contrast of the top two features of Component 1, i.e. (Daylight medium saturation + LMS low saturation) - (Daylight high saturation + S high saturation) are projected onto M1's inflated surface.

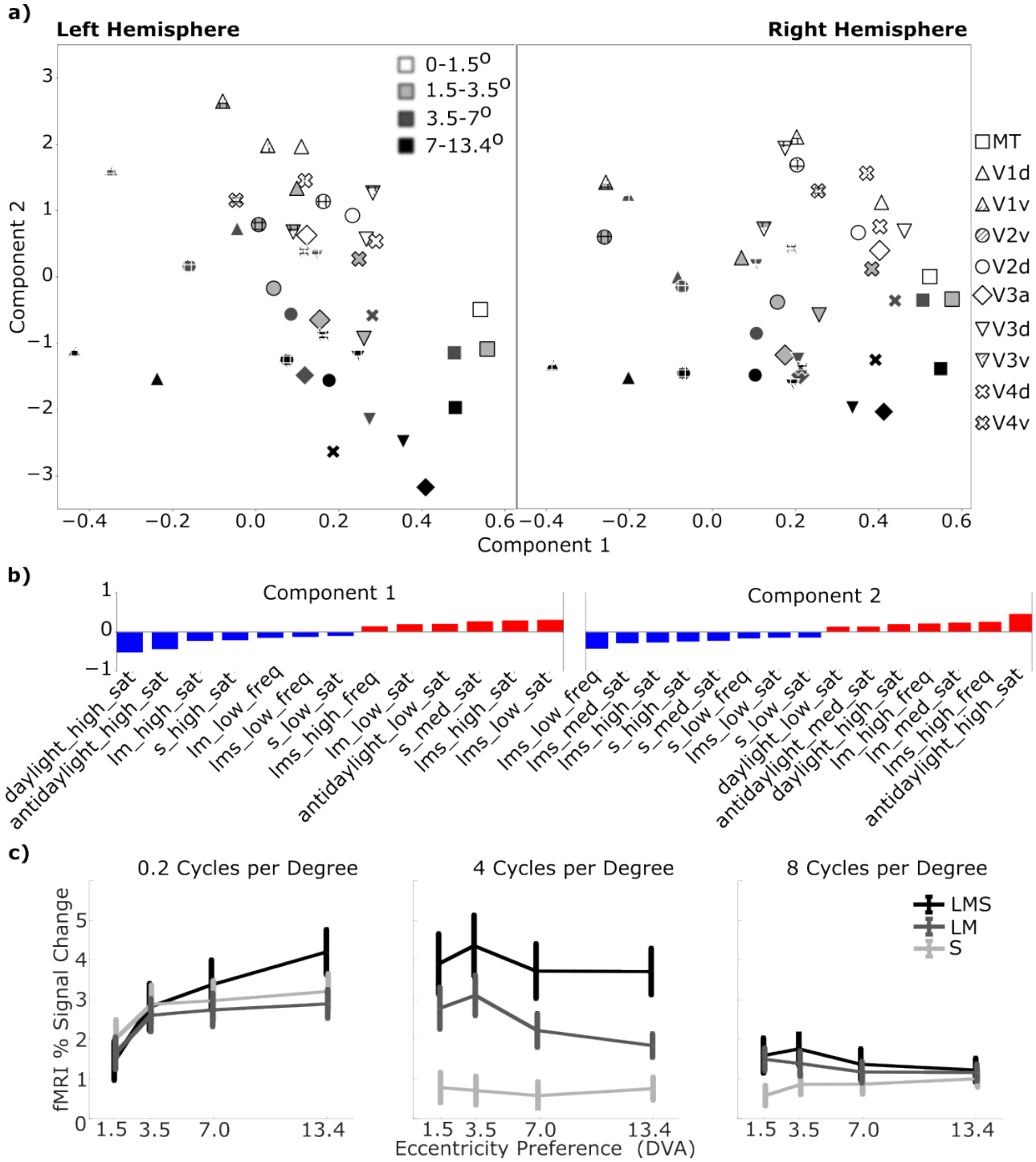

Figure 3. Sparse Linear Discriminant Analysis (sLDA) can differentiate eccentricities. **a)** One sLDA model is fit on all ROIs at all eccentricity levels. Within each ROI, less eccentric voxels have higher average response on component 2. There is some organization of ROIs along component 1, especially MT+, which is clustered on the bottom right. Left and right hemispheres are plotted separately. **b)** The feature weights for the two maximally discriminating components. Features given weight zero are not shown. **c)** fMRI response to gratings of different spatial frequencies as a function of eccentricity across retinotopic areas. For medium and high frequency gratings, LM response drops with eccentricity, while S response remains stable or increases.

Arrangement of retinotopic areas along component 2 suggest that this component separates ventral and dorsal areas, with V1v-V4v possessing more negative values along this axis and V1d-V4d, V3a, and MT+ possessing more positive values. This effect becomes larger along the visual hierarchy. The weight vector for component 2 (Figure 4b) indicates that the ventral/dorsal separability emerges out of a bias for color vs luminance responses, particularly for high saturation Daylight axis colors. This is visualized in figure 4d, effect-size contrast of the top two features of Component 2, i.e. (LMS medium saturation + LMS low saturation) - (Daylight medium saturation + Daylight low saturation) are projected onto M1's inflated surface. The dotted line indicates the boundary between the upper and lower visual hemifields, which were functionally delineated in the separate retinotopic mapping experiments.

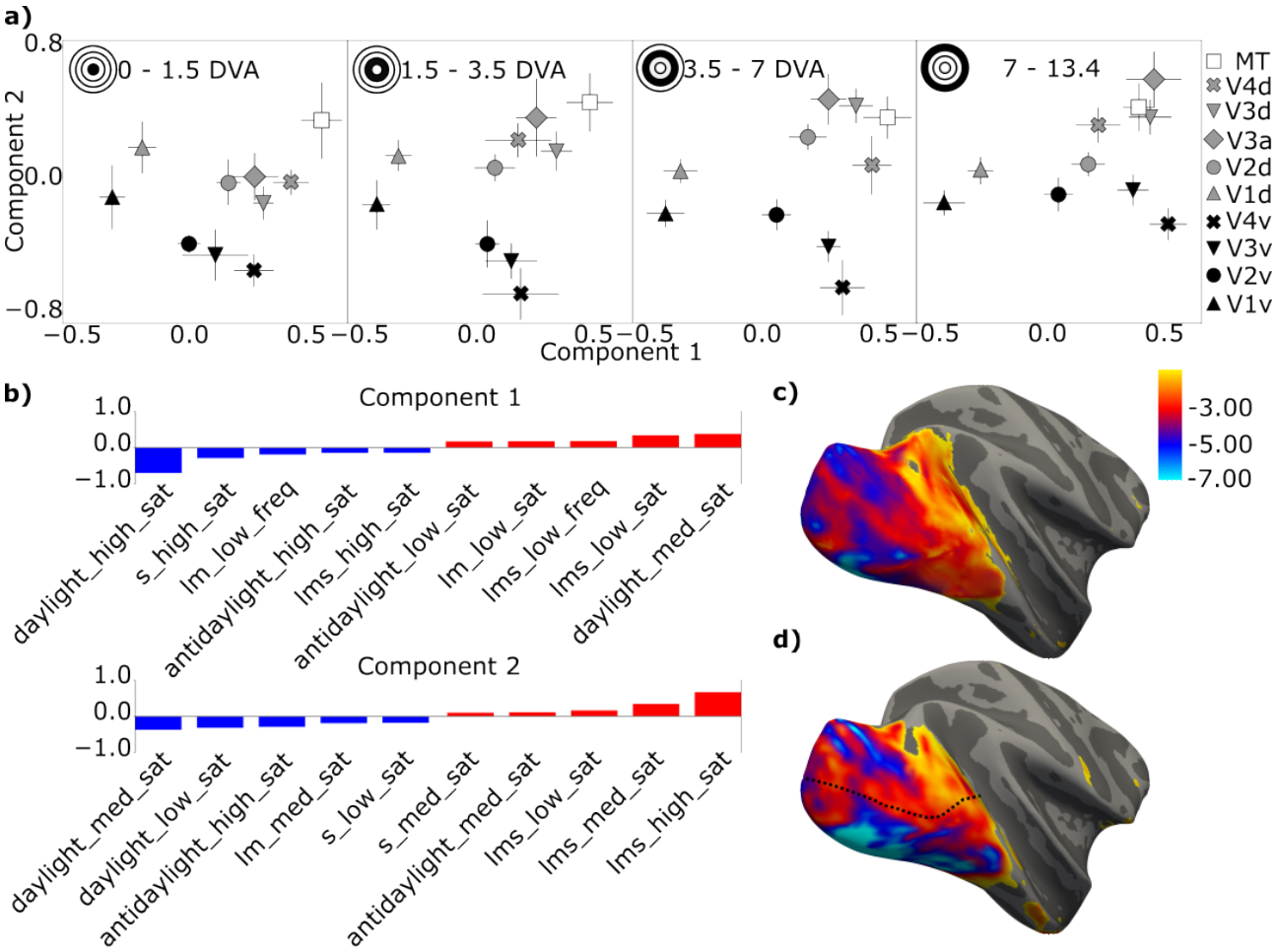

Figure 4. a) One sLDA model was fit considering only distances within each eccentricity level, so as to remove the effects of eccentricity. From left to right, the mean voxel response at each of four eccentricity levels are plotted along the two maximally discriminating components discovered by sLDA. Error bars are 95% confidence intervals via bootstrapping. Independent of eccentricity, ROIs are arranged from posterior to anterior along component 1, and from ventral to dorsal along component 2. **b)** The feature contributions to the two maximally discriminating components. Features given weight zero are not shown. Component 1 roughly corresponds to high vs low or medium saturation gratings, especially on the Daylight axis. Component 2 roughly corresponds to Daylight axis vs greyscale (LMS) gratings. **c)** A surface projection of low and medium vs high saturation gratings (displayed red and blue respectively). Posterior areas show a greater difference in response to low and high saturation gratings. **d)** A surface projection of LMS minus Daylight effect size contrast (displayed red and blue respectively), a generalization of component 2. Daylight is preferred in ventral visual areas. The upper / lower hemifield boundary is denoted with a dotted line.

Again, we further study the effects observed in the sLDA embeddings with univariate analyses. The relationship between anterior and posterior ROIs is corroborated by extracting the slope of the contrast response functions

for each ROI (Figure 5a), revealing that the responses of more anterior regions increase less with higher contrast/saturation gratings than posterior regions. To highlight differences in chromatic response between the ventral and dorsal areas of V1-V4, we plotted the ventral vs dorsal bias for the difference in color and LMS responses across saturations. Explicitly, for a given color grating and saturation level, this metric takes the form

$$Bias = \frac{(Color_v - LMS_v) - (Color_d - LMS_d)}{(Color_v - LMS_v) + (Color_d - LMS_v)} \quad \textbf{(2)}$$

We see that ventral regions have higher $Color - LMS$ responses than dorsal regions, especially for $Daylight - LMS$ (Figure 5b). Daylight axis colors also consistently elicit the strongest responses from retinotopic areas (Figure 5c), suggesting that the $Daylight - LMS$ metric may be most diagnostic for color response overall, and thus for ventral-dorsal separation.

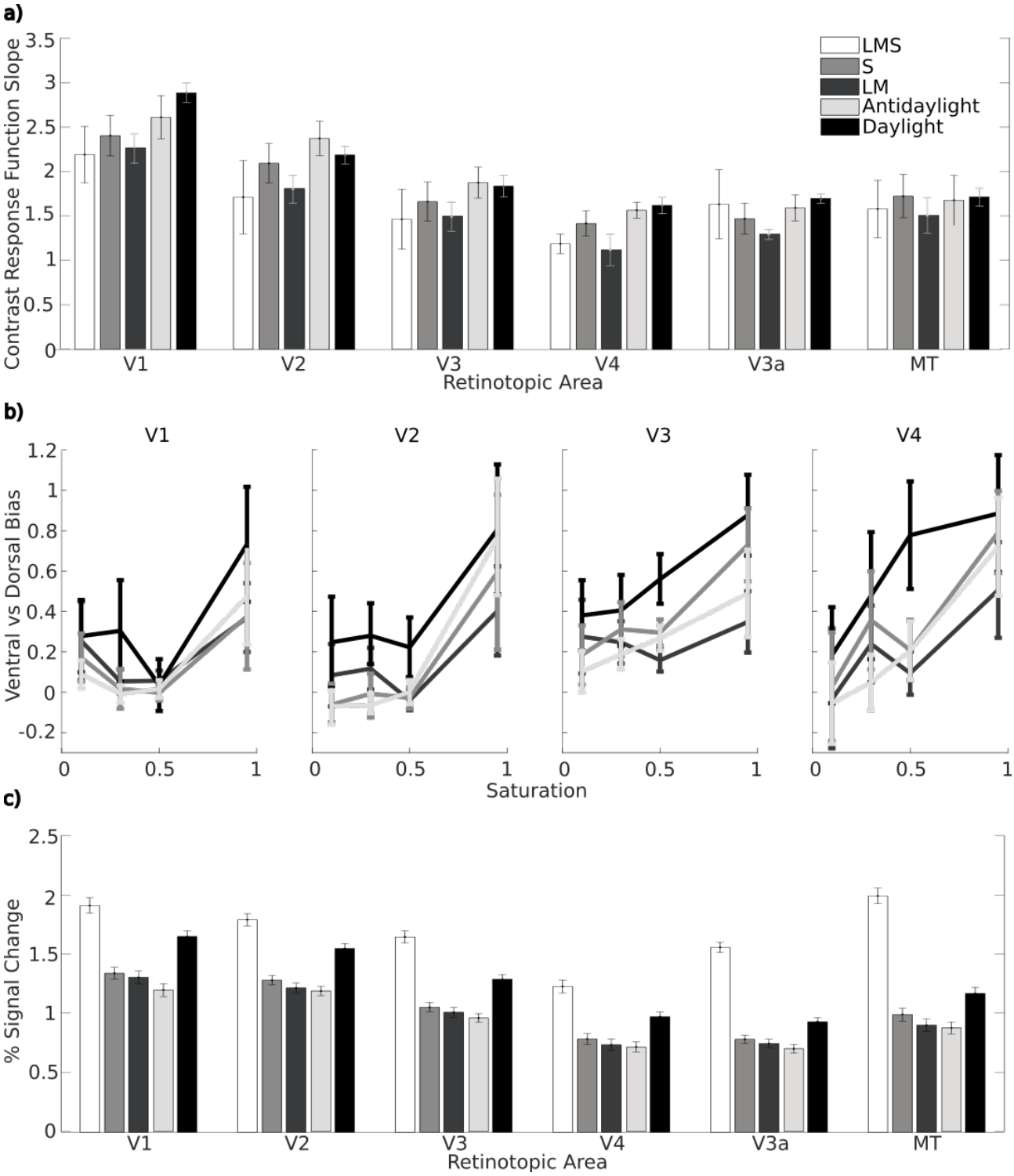

Figure 5. a) Contrast response function slope for each color grating axis across all ROIs. There is a clear downward trend across all regions as we move from V1 to V4, leveling off in V3a and MT+. This trend is clearest for Daylight axis gratings. **b)** Bias for ventral areas (positive) vs dorsal areas (negative) for the difference in color and LMS responses for each color and each saturation level in V1 through V4. Ventral bias is consistent and increases with saturation. The ventral bias is strongest for Daylight vs LMS responses across all regions. **c)** Raw signal change vs background for each color grating, combined across all saturation levels and eccentricities. The Daylight axis consistently has the largest signal of all the colors.

Discussion

Summary of Approach

Using fMRI data obtained in macaque monkeys, we sought to understand how different cortical fields varied in their responses to differences in color, saturation, and spatial frequency. We identified upper and lower visual-field representations and eccentricity representations for V1, V2, V3, V4, and we also identified V3A and MT+. Using a sparse implementation of Linear Discriminant Analysis (sLDA), we identified combinations of colors, saturations, and spatial frequencies that differentiated cortical fields. The approach thereby combines a categorical experimental design (4 color contrast axes x 3 spatial frequencies x 4 saturation levels), with a supervised embedding approach designed to identify interpretable, low dimensional axes in this stimulus space along which the ROIs maximally vary. The results provide insight into the fundamental organization of color, spatial frequency, and saturation across cortical regions and help establish a data-driven multivariate approach to complement traditional univariate analysis for understanding the different contributions that visual areas make to visual processing. We see striking differences in response to chromatic gratings at different eccentricity levels, through the visual hierarchy, and between the upper and lower visual hemifield. Contrasts of Daylight axis colors are a major driver of these differences. This is interesting in the context of work in humans showing that the Daylight axis is especially important for object recognition (Rosenthal et al., 2018; Zito et al., 2016; Lafer-Sousa et al., 2012; Pearce et al., 2014; Winkler et al., 2015; Gegenfurtner and Rieger, 2000).

The multivariate sLDA approach allows us to identify combinations of features that maximally separate retinotopic regions of cortex. In comparison to unsupervised techniques, such as principal component analysis (PCA) and independent component analyses (ICA), which also seek to characterize low-dimensional patterns in high-dimensional data, LDA considers the class labels (here, ROI labels) during decomposition. It is also a complimentary approach to stimuli decoding based characterizations of visual regions used by (Ziemba et al., 2016) to compare V1 and V2. Our specific objective is to identify components (discriminants) that maximize the ratio of between class dispersion to within class dispersion. LDA therefore has a distinct advantage over unsupervised techniques when the goal is to identify interpretable components that discriminate the classes. sLDA has the additional advantage that it supports flexible regularization of the discriminant, encouraging both sparsity, generalizability, and interpretability. This implementation also allows the use of "masking" parameters, which control the extent to which the covariance between different pairs of class labels is considered.

We utilize this feature to fit a single model on all data independent of differences across eccentricity. This removes the overwhelming effect of eccentricity on color response, an effect that could otherwise confound our analysis since the extent of cortical magnification might vary across visual area. For instance LM grating response in MT could be lower than in V1 simply because a higher percentage of voxels respond to peripheral stimuli. By modelling all

eccentricities levels at once, but only considering distances between classes with the same eccentricity level, we construct a basis for separating retinotopic areas that is independent of eccentricity (figure 4).

Summary of Findings

Response to color gratings along the LM, Daylight, Antidaylight axes, as well as to high frequency gratings, were greater for less eccentric cortical voxels, while the response to low and medium frequency luminance and S gratings were more stable into the periphery. This is consistent with fMRI and behavioral findings in humans (D'Souza et al., 2016; Mullen et al., 2005), and with predictions based on retinal photo-receptor distributions (Cornish et al., 2004). While this relationship is strongly conserved within each visual area, it is not necessarily conserved between them, e.g. peripheral areas of V4 show greater response to LM and Daylight gratings than foveal areas of MT+ (figure 3).

We also find that anterior and posterior areas could be differentiated mostly by response to different color saturation levels. V1 is much more biased toward high saturation Daylight axis gratings over medium or low saturation Daylight gratings than other areas, causing it to be highly separated along component 1 in the sLDA embedding displayed in figure 4. CRF slope decreases along the visual hierarchy (figure 5a), though for many color axes V1 and V2 are not found to be significantly different. This matches results found in humans (Yan et al., 2014; Vinke et al., 2021), showing a decrease in CRF slope from V1 to V2 to V3. Despite difference in color response across eccentricity levels, the relationship between CRFs of retinotopic areas remains consistent.

Finally, we find that ventral visual areas have a different color response profile than dorsal visual areas. Ventral areas appear to have significantly stronger bias toward Daylight axis gratings over LMS gratings than dorsal areas. To our knowledge, this is the first time this effect has been identified. Wade et al. (2008) found that in Macaque V4 specifically there was no significant difference in response to LM and S axis colors across ventral and dorsal subdivisions. However they did not measure responses to colors that modulate the intermediate Daylight or Antidaylight axes, which are the stimuli that most strongly separate dorsal and ventral areas; and neither do they control for eccentricity, which may conceal differences in LM and S tuning in the fovea and the periphery across the dorsal/ventral split. Other work provides some evidence for perceptual differences across the upper and lower visual hemifields. (Zito et al., 2016; Denman et al., 2018).

Color responses along the Daylight axis seem particularly useful for parcellating visual cortex. The slope of the contrast response function in response to Daylight axis colors steadily decreased as one goes from V1 to the more anterior regions of V4, V3a, and MT+ (Figure 5a). Additionally, the difference in response between luminance and Daylight axis colors separates dorsal and ventral regions (Figure 5b). Colors along the Daylight axis and Antidaylight axis are produced by a combination of subcortical cone-opponent channels, which, when matched according to cone-contrast, should be indistinguishable by the responses of these channels. Previous work has found asymmetries in the responses to the Daylight and Antidaylight colors in visual cortex, revealing separate

cortical processing for these colors; a fRMI study in humans found a preferential response to Antidaylight colors in V1, V2, V3, hV4, V3AB, and VO (Goddard et al., 2010a), while fMRI and electrophysiological work in macaques found a bias towards Daylight colors in V1 (Lafer-Sousa et al., 2012). Our work, consistent with the previous macaque study, similarly finds a bias towards Daylight colors compared to Antidaylight colors, not only in V1 but in all retinotopic regions (Figure 5). The steady decline in the slope of the Daylight axis contrast response function as one moves posterior to anterior may be the result of non-linear transformations of the cone-opponent signals, resulting in greater and more even color selectivity in later visual areas (Conway, 2014). The heightened Daylight color response and its ability to separate dorsal and ventral regions may have functional significance; (Rosenthal et al., 2018) found that warm / cool color contrast along the Daylight axis are most useful for distinguishing objects from the background, and that color biased regions in IT and V4 are more responsive to Daylight axis colors, suggesting that ventral-anterior areas may utilize their increased sensitivity to Daylight axis colors to facilitate object recognition, and that this sensitivity is inherited from earlier in the visual pathway.

Relationship to Human Studies

In many ways, our findings are consistent with results reported in human subjects. Yan et al. (2014), for instance, have reported that human early visual areas are more sensitive to contrast change than more anterior areas, consistent our result indicating that posterior areas have higher contrast response functions than anterior areas (Figure 5a). Mullen et al. (2007) found that BOLD response to LM axis colors tends to decrease faster with eccentricity than S axis colors. Similarly, Mullen et al. (2005) reported that sensitivity to LM stimuli decreases until roughly 25° visual field angle at which point they are nearly undetectable. They also reported that sensitivity to S and LMS stimuli decreases more slowly. This matches our findings showing the MION response to LM gratings falls off with eccentricity, while response to S gratings remains steady or increases, for medium and high spatial frequency conditions. There is also evidence of functional differences between ventral and dorsal areas. Zito et al. (2016), for example, found that human object recognition is enhanced for stimuli in the upper visual field, while motion detection is enhanced for objects in lower visual field. Similarly, Denman et al. (2018) found that mice are sensitive to stimuli chromaticity in the upper, but not lower, visual field.

Future Directions

Shared visual statistics and (gross) similarities in ecological pressures shared between species (e.g., object and scene identification, sexual selection, foraging) likely helped preserve these relationships in the neural organization of retinotopic and color information across evolutionary timescales (80m years between mouse and human, and 23m years between macaque and human). Better understanding of the role of color in the computations performed in different retinotopic regions will require better understanding of the visual statistics of the visual world. For instance,

are objects of interest in the upper visual field more likely to have useful information on the Daylight axis than objects in the lower visual field?

Conclusion

Using sparse Linear Discriminant Analysis, we identified low dimensional axes in visual feature space (i.e., sparse combinations of features) that maximally differentiate regions of interest. We found that response to Antidaylight, Daylight, and LM gratings decrease more rapidly with increasing eccentricity than responses to low and medium frequency S gratings. The difference in response between high and low saturation gratings was greatest in V1, decreasing along the visual hierarchy.

These findings are consistent with results from human psychophysical results, which indicate that detection thresholds for LM contrast decrease with eccentricity. They are also consistent with past fMRI studies, which have found that BOLD response to LM contrast decreases with increasing eccentricity, and that BOLD response is more different across saturation levels for regions earlier in the visual hierarchy.

We also find that ventral areas are more biased toward Daylight axis than dorsal areas, suggesting that color information in the upper and lower hemifield is used in different ways. This bias become more pronounced as we move from V1 to V4.

A. Author Contributions

S.R.L. developed the sLDA approach, drafted the manuscript, and contributed to data analysis and fMRI processing. S.J.D drafted the manuscript, prepared the data for analysis, and contributed to data analysis and fMRI processing. K.B. provided advice on methods and drafted and reviewed the manuscript. C.R.B. conceived of the basic experimental design, provided advice, and reviewed the manuscript.

Bibliography

Beauchamp, M. S., Haxby, J. V., Jennings, J. E., and DeYoe, E. A. (1999). An fMRI Version of the Farnsworth–Munsell 100-Hue Test Reveals Multiple Color-selective Areas in Human Ventral Occipitotemporal Cortex. *Cerebral Cortex*, 9(3):257–263.

Brewer, A. A., Liu, J., Wade, A. R., and Wandell, B. A. (2005). Visual field maps and stimulus selectivity in human ventral occipital cortex. *Nature neuroscience*, 8(8):1102–1109.

Callaghan, T. C. (1984). Dimensional interaction of hue and brightness in preattentive field segregation. *Perception & psychophysics*, 36(1):25–34.

Cant, J. S. and Goodale, M. A. (2006). Attention to Form or Surface Properties Modulates Different Regions of Human Occipitotemporal Cortex. *Cerebral Cortex*, 17(3):713–731.

Conway, B. R. (2009). Color vision, cones, and color-coding in the cortex. *The Neuroscientist*, 15(3):274–290. PMID: 19436076.

Conway, B. R. (2014). Color signals through dorsal and ventral visual pathways. *Visual Neuroscience*, 31(2):197–209.

Conway, B. R. (2018). The organization and operation of inferior temporal cortex. *Annual review of vision science*, 4:381.

Cornish, E. E., Hendrickson, A. E., and Provis, J. M. (2004). Distribution of short-wavelength-sensitive cones in human fetal and postnatal retina: early development of spatial order and density profiles. *Vision Research*, 44(17):2019–2026.

Denman, D. J., Luviano, J. A., Ollerenshaw, D. R., Cross, S., Williams, D., Buice, M. A., Olsen, S. R., and Reid, R. C. (2018). Mouse color and wavelength-specific luminance contrast sensitivity are non-uniform across visual space. *eLife*, 7.

Derrington, A. M., Krauskopf, J., and Lennie, P. (1984). Chromatic mechanisms in lateral geniculate nucleus of macaque. *The Journal of Physiology*, 357(1):241–265.

D'Souza, D. V., Auer, T., Frahm, J., Strasburger, H., and Lee, B. B. (2016). Dependence of chromatic responses in v1 on visual field eccentricity and spatial frequency: An fmri study. *Journal of the Optical Society of America A*, 33(3):A53.

Enroth-Cugell, C. and Robson, J. G. (1966). The contrast sensitivity of retinal ganglion cells of the cat. *The Journal of physiology*, 187(3):517–552.

Essen, D. V. and Zeki, S. (1978). The topographic organization of rhesus monkey prestriate cortex. *The Journal of physiology*, 277(1):193–226.

Gattass, R., Sousa, A., and Gross, C. (1988). Visuotopic organization and extent of v3 and v4 of the macaque. *Journal of Neuroscience*, 8(6):1831–1845.

Gegenfurtner, K. R. and Rieger, J. (2000). Sensory and cognitive contributions of color to the recognition of natural scenes. *Current Biology*, 10(13):805–808.

Goddard, E., Mannion, D. J., McDonald, J. S., Solomon, S. G., and Clifford, C. W. G. (2010a). Combination of subcortical color channels in human visual cortex. *Journal of Vision*, 10(5):25–25.

Goddard, E., Solomon, S., and Clifford, C. (2010b). Adaptable mechanisms sensitive to surface color in human vision. *Journal of Vision*, 10(9):17–17.

Harada, T., Goda, N., Ogawa, T., Ito, M., Toyoda, H., Sadato, N., and Komatsu, H. (2009). Distribution of colour-selective activity in the monkey inferior temporal cortex revealed by functional magnetic resonance imaging. *European Journal of Neuroscience*, 30(10):1960–1970.

Hass, C. A., Angueyra, J. M., Lindbloom-Brown, Z., Rieke, F., and Horwitz, G. D. (2015). Chromatic detection from cone photoreceptors to V1 neurons to behavior in rhesus monkeys. *Journal of Vision*, 15(15):1–1.

Horwitz, G. D. (2020). Signals related to color in the early visual cortex. *Annual Review of Vision Science*, 6(1):287–311. PMID: 32936735.

Horwitz, G. D., Chichilnisky, E. J., and Albright, T. D. (2005). Blue-yellow signals are enhanced by spatiotemporal luminance contrast in macaque v1. *Journal of Neurophysiology*, 93(4):2263–2278. PMID: 15496484.

Johnson, E. N., Hawken, M. J., and Shapley, R. (2004). Cone inputs in macaque primary visual cortex. *Journal of Neurophysiology*, 91(6):2501–2514. PMID: 14749310.

Kaas, J. H. (1993). The functional organization of somatosensory cortex in primates. *Annals of Anatomy-Anatomischer Anzeiger*, 175(6):509–518.

Kaas, J. H. (2013). The evolution of brains from early mammals to humans. *Wiley Interdisciplinary Reviews: Cognitive Science*, 4(1):33–45.

Khosla, M., Ratan Murty, N. A., and Kanwisher, N. (2022). A highly selective response to food in human visual cortex revealed by hypothesis-free voxel decomposition. *Current Biology*, 32(19):4159–4171.e9.

Kingma, D. P. and Ba, J. (2014). Adam: A method for stochastic optimization.

Kolster, H., Mandeville, J. B., Arsenault, J. T., Ekstrom, L. B., Wald, L. L., and Vanduffel, W. (2009). Visual field map clusters in macaque extrastriate visual cortex. *Journal of Neuroscience*, 29(21):7031–7039.

Lafer-Sousa, R. and Conway, B. R. (2013). Parallel, multi-stage processing of colors, faces and shapes in macaque inferior temporal cortex. *Nature neuroscience*, 16(12):1870–1878.

Lafer-Sousa, R., Conway, B. R., and Kanwisher, N. G. (2016). Color-biased regions of the ventral visual pathway lie between face-and place-selective regions in humans, as in macaques. *Journal of Neuroscience*, 36(5):1682–1697.

Lafer-Sousa, R., Liu, Y. O., Lafer-Sousa, L., Wiest, M. C., and Conway, B. R. (2012). Color tuning in alert macaque v1 assessed with fmri and single-unit recording shows a bias toward daylight colors. *JOSA A*, 29(5):657–670.

Lennie, P., Krauskopf, J., and Sclar, G. (1990). Chromatic mechanisms in striate cortex of macaque. *Journal of Neuroscience*, 10(2):649–669.

Liu, J. and Wandell, B. A. (2005). Specializations for chromatic and temporal signals in human visual cortex. *Journal of Neuroscience*, 25(13):3459–3468.

MacLeod, D. I. and Boynton, R. M. (1979). Chromaticity diagram showing cone excitation by stimuli of equal luminance. *Journal of the Optical Society of America*, 69(8):1183.

Movshon, J. A., Thompson, I. D., and Tolhurst, D. J. (1978). Spatial summation in the receptive fields of simple cells in the cat's striate cortex. *The Journal of physiology*, 283:53–77.

Mullen, K. T. (2019). The response to colour in the human visual cortex: The fmri approach. *Current Opinion in Behavioral Sciences*, 30:141–148.

Mullen, K. T., Dumoulin, S. O., McMahon, K. L., De Zubicaray, G. I., and Hess, R. F. (2007). Selectivity of human retinotopic visual cortex to s-cone-opponent, l/m-cone-opponent and achromatic stimulation. *European Journal of Neuroscience*, 25(2):491–502.

Mullen, K. T., Sakurai, M., and Chu, W. (2005). Does l/m cone opponency disappear in human periphery? *Perception*, 34(8):951–959.

Paxinos, G., Huang, X.-F., and Toga, A. W. (2000). The rhesus monkey brain in stereotaxic coordinates.

Pearce, B., Crichton, S., Mackiewicz, M., Finlayson, G. D., and Hurlbert, A. (2014). Chromatic illumination discrimination ability reveals that human colour constancy is optimised for blue daylight illuminations. *PLOS ONE*, 9(2):1–10.

Pennock, I. M. L., Racey, C., Allen, E., Wu, Y., Naselaris, T., Kay, K., Franklin, A., and Bosten, J. (2022). Color-biased regions in the ventral visual pathway are food-selective. *bioRxiv*.

Pihlaja, M., Henriksson, L., James, A. C., and Vanni, S. (2008). Quantitative multifocal fmri shows active suppression in human v1. *Human Brain Mapping*, 29(9):1001–1014.

Reveley, C., Gruslys, A., Ye, F. Q., Glen, D., Samaha, J., E. Russ, B., Saad, Z., K. Seth, A., Leopold, D. A., and Saleem, K. S. (2016). Three-Dimensional Digital Template Atlas of the Macaque Brain. *Cerebral Cortex*, 27(9):4463–4477.

Rilling, J. K. (2014). Comparative primate neuroimaging: insights into human brain evolution. *Trends in cognitive sciences*, 18(1):46–55.

Rosa, M. G. and Tweedale, R. (2005). Brain maps, great and small: lessons from comparative studies of primate visual cortical organization. *Philosophical Transactions of the Royal Society B: Biological Sciences*, 360(1456):665–691.

Rosenthal, I., Ratnasingam, S., Haile, T., Eastman, S., Fuller-Deets, J., and Conway, B. R. (2018). Color statistics of objects, and color tuning of object cortex in macaque monkey. *Journal of Vision*, 18(11).

Singh, K. D., Smith, A., and Greenlee, M. W. (2000). Spatiotemporal frequency and direction sensitivities of human visual areas measured using fmri. *Neuroimage*, 12(5):550–564.

Stockman, A. and Sharpe, L. T. (2000). The spectral sensitivities of the middle- and long-wavelength-sensitive cones derived from measurements in observers of known genotype. *Vision Research*, 40(13):1711–1737.

Sumner, P. and Mollon, J. D. (2000). Chromaticity as a signal of ripeness in fruits taken by primates. *Journal of Experimental Biology*, 203(13):1987–2000.

Surridge, A. K., Osorio, D., and Mundy, N. I. (2003). Evolution and selection of trichromatic vision in primates. *Trends in Ecology & Evolution*, 18(4):198–205.

Van Essen, D. C. (2004). Surface-based approaches to spatial localization and registration in primate cerebral cortex. *Neuroimage*, 23:S97–S107.

Vanduffel, W., Fize, D., Mandeville, J. B., Nelissen, K., Van Hecke, P., Rosen, B. R., Tootell, R. B., and Orban, G. A. (2001). Visual motion processing investigated using contrast agent-enhanced fmri in awake behaving monkeys. *Neuron*, 32(4):565–577.

Vinke, L. N., Bloem, I. M., and Ling, S. (2021). Saturating nonlinearities of contrast response in human visual cortex. *The Journal of Neuroscience*, 42(7):1292–1302.

Vizioli, L., Moeller, S., Dowdle, L., Akçakaya, M., De Martino, F., Yacoub, E., and Uğurbil, K. (2021). Lowering the thermal noise barrier in functional brain mapping with magnetic resonance imaging. *Nature Communications*, 12.

Wade, A., Augath, M., Logothetis, N., and Wandell, B. (2008). fmri measurements of color in macaque and human. *Journal of vision*, 8(10):6–6.

Wade, A. R., Brewer, A. A., Rieger, J. W., and Wandell, B. A. (2002). Functional measurements of human ventral occipital cortex: retinotopy and colour. *Philosophical Transactions of the Royal Society of London. Series B: Biological Sciences*, 357(1424):963–973.

Wandell, B. A. and Winawer, J. (2011). Imaging retinotopic maps in the human brain. *Vision research*, 51(7):718–737.

Winkler, A. D., Spillmann, L., Werner, J. S., and Webster, M. A. (2015). Asymmetries in blue–yellow color perception and in the color of 'the dress'. *Current Biology*, 25(13):R547–R548.

Witzel, C. and Gegenfurtner, K. R. (2018). Color perception: Objects, constancy, and categories. *Annual Review of Vision Science*, 4:475–499.

Xanthopoulos, P., Pardalos, P. M., and Trafalis, T. B. (2013). *Linear Discriminant Analysis*, pages 27–33. Springer New York, New York, NY.

Yan, T., Wang, B., Geng, Y., Yan, Y., Mu, N., Wu, J., Guo, Q., Tang, X., Zeng, Y., and Peng, Y. (2014). Contrast response functions with wide-view stimuli in the human visual cortex. *Perception*, 43(7):677–693.

Zeki, S., Watson, J., Lueck, C., Friston, K. J., Kennard, C., and Frackowiak, R. (1991). A direct demonstration of functional specialization in human visual cortex. *Journal of neuroscience*, 11(3):641–649.

Ziemba, C. M., Freeman, J., Movshon, J. A., and Simoncelli, E. P. (2016). Selectivity and tolerance for visual texture in macaque v2. *Proceedings of the National Academy of Sciences*, 113(22).

Zito, G. A., Cazzoli, D., Müri, R. M., Mosimann, U. P., and Nef, T. (2016). Behavioral differences in the upper and lower visual hemifields in shape and motion perception. *Frontiers in Behavioral Neuroscience*, 10.